Astronomy & Astrophysics manuscript no. aanda
October 9, 2025

The rise and fall of Little Red Dots could be driven by the environment

Rosa M. Mérida[1], Gaia Gaspar[1,2], Yoshihisa Asada[1,3,4,5], Marcin Sawicki[1], Kiyoaki Christopher Omori[1], Chris J. Willot[6], Nicholas S. Martis[7], Adam Muzzin[8], Gaël Noirot[9], Gregor Rihtaršič[7], Ghassan T. E. Sarrouh[8], and Roberta Tripodi[10]

[1] Institute for Computational Astrophysics and Department of Astronomy and Physics, Saint Mary's University, 923 Robie Street, Halifax, NS B3H 3C3, Canada
e-mail: Rosa.MeridaGonzalez@smu.ca
[2] Observatorio Astronómico de Córdoba, Universidad Nacional de Córdoba, Laprida 854, X5000, Córdoba, Argentina
[3] Dunlap Institute for Astronomy and Astrophysics, 50 St. George Street, Toronto, Ontario, M5S 3H4, Canada
[4] Waseda Research Institute for Science and Engineering, Faculty of Science and Engineering, Waseda University, 3-4-1 Okubo, Shinjuku, Tokyo 169-8555, Japan
[5] Department of Astronomy, Kyoto University, Sakyo-ku, Kyoto 606-8502, Japan
[6] National Research Council of Canada, Herzberg Astronomy & Astrophysics Research Centre, 5071 West Saanich Road, Victoria, BC, V9E 2E7, Canada
[7] Faculty of Mathematics and Physics, Jadranska ulica 19, SI-1000 Ljubljana, Slovenia
[8] Department of Physics and Astronomy, York University, 4700 Keele St. Toronto, Ontario, M3J 1P3, Canada
[9] Space Telescope Science Institute, 3700 San Martin Drive, Baltimore, Maryland 21218, USA
[10] INAF - Osservatorio Astronomico di Roma, Via Frascati 33, Monte Porzio Catone, 00078, Italy

Received September 15, 1996; accepted March 16, 1997

ABSTRACT

The Little Red Dot (LRD) paradigm comprises three main unknowns that are intrinsically connected: (1) What is the nature of these sources? (2) How do they form? (3) How do they evolve? Larger spectroscopic samples and high-resolution data are needed to delve deeper into the mechanisms ruling these sources. Understanding their formation and evolution requires identifying the rise and fall of the key features that characterize these systems, such as their compactness and "V"-shaped spectral energy distributions. In this work, we present a galaxy system nicknamed *The Stingray* that was identified in the Canadian NIRISS Unbiased Cluster Survey (CANUCS). This group contains three sources at $z_{\rm spec} = 5.12$, including an active galactic nucleus (AGN), a Balmer break galaxy, and a star-forming satellite. The latter resembles a Building Block System in which interactions boost stellar mass and black hole mass growth beyond what is expected from secular processes alone. The AGN in this system exhibits features indicative of a transitional object, bridging a normal AGN and an LRD phase. These are a blue rest-frame ultraviolet slope, compact size, and a broad Hα line (all of which are characteristic of LRDs), but a flatter rest-frame optical slope compared to that observed in LRDs. The features in this source point to the emergence or fading of an LRD, potentially triggered by environmental effects.

Key words. Galaxies: interactions – active – high-redshift – evolution

1. Introduction

Two years after the discovery of the so-called Little red dots (LRDs; Labbé et al. 2023, Barro et al. 2024, Greene et al. 2024, Matthee et al. 2024) by the JWST (Gardner et al. 2023), our understanding of their formation, evolution, and properties remains highly incomplete. Consistent features across all studies of these intriguing sources are their compact nature, the presence of broad Balmer emission lines, and a distinctive "V"-shaped spectral energy distribution (SED). This SED is characterized by a nearly flat to blue rest-frame ultraviolet (UV) continuum, followed by a steep optical slope. However, identifying the complete sample of such sources remains challenging: photometric selections can be contaminated by emission lines that mimic steep spectral slopes (Hainline et al. 2025). Moreover, they can also overlook objects that reveal "V"-shaped continua only through spectroscopy (Hviding et al. 2025).

Different combinations of models were proposed to explain the nature of these objects, including active galactic nuclei (AGN), stellar emission, and composite models (e.g., Inayoshi & Maiolino 2025, Pérez-González et al. 2024, Greene et al. 2024, Tripodi et al. 2024, Mérida et al. 2025a). None of the latter have been able to fully reproduce the bulk of the LRD population and their challenging properties, which include a lack of X-ray detections (Ananna et al. 2024), absence of emission from a dusty torus at longer wavelengths (Setton et al. 2025), or lack of variability (Zhang et al. 2024). As a result, more exotic solutions arose, such as the black hole star (BH*) model (e.g., de Graaff et al. 2025b, Naidu et al. 2025, Ji et al. 2025, Rusakov et al. 2025) or binary massive black holes (Inayoshi et al. 2025b). However, larger spectroscopic samples and high-resolution observations are still required to further investigate any of these hypotheses.

Another key aspect of the LRD paradigm is the emergence and evolution of these sources. Although there are now candidates of $z \sim 0$ LRD relics (see Lin et al. 2025), the population of these sources has been shown to exhibit a dramatic drop in their number density at $z \sim 4$ ($1 - 2$ dex from $z \sim 4$ to $z \sim 2$; Ko-

cevski et al. 2025, Inayoshi 2025, Ma et al. 2025, Zhuang et al. 2025). The evolutionary pathway followed by these sources has not been fully elucidated yet.

According to Billand et al. (2025), LRDs are a phase in galaxy evolution, which implies there must be transition stages in which galaxies exhibit LRD features while simultaneously developing new characteristics. These authors also affirm that cold accretion may lead to an increase in the stellar mass ($M_\star$), which makes LRDs lose their genuine "V"-shape and compactness as these stars form and populate the galaxy outskirts. In that same work, mergers are also proposed as channels for the disruption of the LRD phase.

There are already observations of LRDs in dense environments, including LRDs in pairs (Tanaka et al. 2024, Mérida et al. 2025a), LRDs in galaxy overdensities (Labbe et al. 2024, Rinaldi et al. 2024), and star clusters or nebular gas close to LRDs (Chen et al. 2025). In Mérida et al. (2025a) we presented evidence of a synchronous evolution of an LRD pair at $z \sim 7$ and the key role played by the environment in the triggering and quenching of these objects.

There are likely different channels for the formation and destruction of LRDs, and environmental effects should be considered as potential drivers of some of these channels. To understand how LRDs are triggered and how they disappear, it is key to investigate the properties of transitional objects. The presence of these sources can be linked to the end of an LRD phase, as well as to the emergence of one or several LRD phases along a galaxy's lifetime.

In this work, we report the discovery of a transitional object, bridging normal AGNs and LRDs, embedded in a galaxy system nicknamed *The Stingray* at $z_{\rm spec} = 5.12$. This group contains what we named a transitional LRD (tLRD), a Balmer break galaxy (BBG), and a star-forming satellite. They all show signs of coordinated star formation histories (SFHs), resembling the Building Blocks System (BBS; Asada et al. in prep). In such systems, stellar mass ($M_\star$) growth can be dramatically enhanced by interaction-triggered bursts of star formation.

Throughout this work we assume $\Omega_{\rm M,0} = 0.3$, $\Omega_{\Lambda,0} = 0.7$, and $\rm H_0 = 70\ km\ s^{-1}\ Mpc^{-1}$. In this cosmology, the Universe is 1.145 Gyr old at $z = 5.12$, with $1''$ being equivalent to 6.3 kpc. We use AB magnitudes (Oke & Gunn 1983) and all $M_\star$ and star formation rate (SFR) estimates assume a Chabrier (2003) initial mass function (IMF).

2. Data

This work is based on data from the Canadian NIRISS Unbiased Cluster Survey (CANUCS; GTO program #1208; Willott et al. 2022), consisting of Near Infrared Camera (NIRCam; Rieke et al. 2023) and JWST Near InfraRed Imager and Slitless Spectrograph (NIRISS; Doyon et al. 2023) observations of five strong lensing clusters and five flanking fields (where lensing magnification is negligible). CANUCS also incorporates Near Infrared Spectrograph (NIRSpec; Jakobsen et al. 2022) PRISM follow-up in all the fields and medium resolution spectroscopy using the Micro-Shutter Assembly (MSA) in the MACS1149 flanking field, where our galaxy system is located.

This field was observed with the NIRCam broadband filters $F090W$, $F115W$, $F150W$, $F277W$, $F444W$, and medium band filters $F140M$, $F210M$, $F300M$, $F335M$, $F360M$, $F410M$. The Cycle 2 "JWST in Technicolor" program (GO program #3362, PI: A. Muzzin) added observations in the $F070W$, $F164N$, $F187N$, $F200W$, $F356W$, $F430M$, $F460M$, and $F480M$ filters. It was also observed with the Advanced Camera for Surveys (ACS) ($F435W$, $F606W$, $F814W$) and the Wide Field Camera 3 (WFC3) (namely $F105W$, $F125W$, $F140W$, and $F160W$) onboard HST. More information regarding CANUCS/Technicolor reduction, calibration, and photometric products can be found in Sarrouh et al. (2025) and references therein.

Table 1: Coordinates and redshifts of the galaxies presented in this work.

Source	RA	dec	photo-z	spec-z
tLRD	11:49:33.732	+22:16:06.892	5.21	5.1245
BBG	11:49:33.688	+22:16:06.352	5.26	5.1258
SAT1	11:49:33.656	+22:16:06.717	5.21	5.1238
C1	11:49:33.725	+22:16:06.754	5.22	-
C2	11:49:33.708	+22:16:06.813	0.80	-
C3	11:49:33.686	+22:16:06.838	0.78	-

Our galaxies were also observed during the Cycle 3 CANUCS follow-up (GTO program 4527 on 18 May 2025) with the NIRSpec G395M medium-resolution grating in 2 MSA configurations with ~ 3.1 ks exposures each. Initial processing utilized the STScI `jwst` stage 1 pipeline with custom snowball and $1/f$ noise correction. The `jwst` stage 2 pipeline was run up to the photometric calibration step. Then, we used the `grizli` and `msaexp` (Brammer 2022, 2023) packages. Wavelength calibration applied a correction for the known intra-shutter offset along the dispersion direction. One-dimensional spectra were obtained using a wavelength-dependent optimal extraction that accounts for the increase in the point-spread function full width at half maximum with wavelength. Further details about the NIRSpec MSA data processing can be found in Heintz et al. (2025) and Sarrouh et al. (2025).

The slit configuration is displayed in Fig. 1. One of the slits was poorly aligned with the centroid of one of the sources, so the scaling correction, based on photometry, for that spectrum was larger. Due to the crowded nature of the system, background subtraction was customized and performed using slits less prone to contamination from nearby sources.

3. *The Stingray*

3.1. Discovery and basic properties

This galaxy group was identified in the CANUCS photometric catalog (Sarrouh et al. 2025) and targeted for NIRSpec follow-up. It is located within a $z = 5.12 \pm 0.03$ overdensity and its main component, which we named CANUCS-MACS1149-tLRD, shows $F300M$ and $F410M$ excess compatible with prominent Hβ+[OIII] and Hα emission lines.

The group was dubbed *The Stingray*, and consists of at least 3 galaxies at $z = 5.12$ for which we have NIRSpec MSA data, namely CANUCS-MACS1149-tLRD, -BBG, and -SAT1 (see labels in Fig. 1). The $z_{\rm spec}$ values for all three galaxies were derived based on the Hα emission lines in their spectra. The tLRD and BBG sources are separated by 5.1 kpc; there are 2.7 kpc between BBG and SAT1; and SAT1 and the tLRD are 3.8 kpc away.

We used `SExtractor` (Bertin & Arnouts 1996) to recover the centroids of potential sources in the vicinity, identifying three companions, C1, C2, and C3, along with a fuzzy structure centered at C2. There is also another galaxy group to the north (pink arrow in Fig. 1), $\sim 1.3''$ away from the tLRD. This galaxy group on top is likely a $z \sim 1.5$ system according to the photometric redshifts derived with `EAzY` (Brammer et al. 2008). Only photometric data are available for the aforementioned sources.

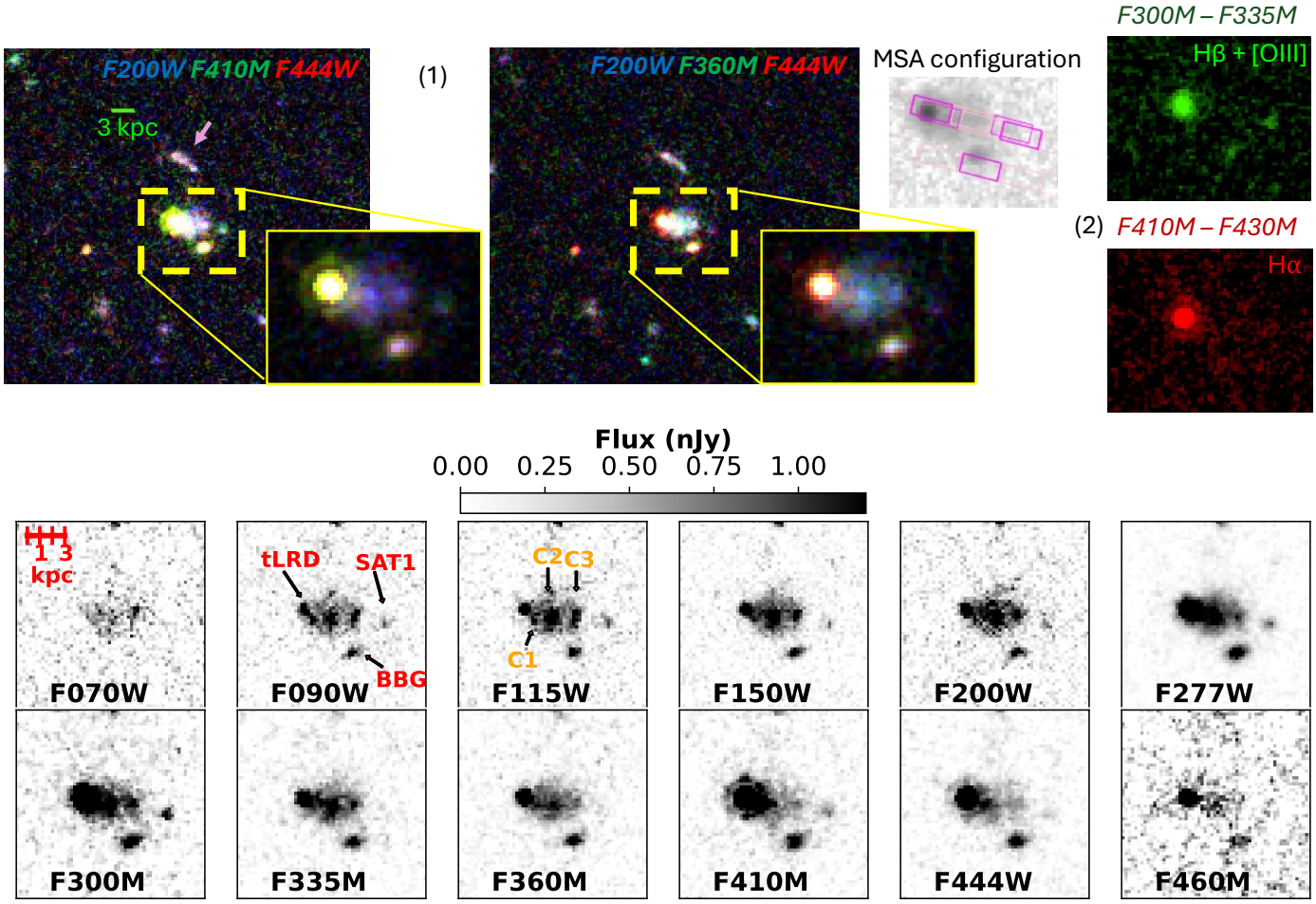

Fig. 1: Cutouts of the galaxy group in different bands. Top: (1) 7.7×7.1 arcsec^2 cutouts of two RGB images based on $F200W$, $F410M$, and $F444W$ (left) and $F200W$, $F360M$, and $F444W$ (right) NIRCam imaging, not convolved to $F444W$ resolution. The yellow square encloses the region that contains the part of the Stingray studied in this work; its dimensions are 2.0×1.4 arcsec^2. We include a view in a less saturated scale to spotlight the difference in color between the different galaxies. These images highlight the $F410M$ excess in the tLRD (see panel 2), due to Hα emission at this z, with respect to the continuum probed by $F360M$. The pink arrow in the left panel points to a $z \sim 1.5$ galaxy group $\sim 1.3''$ away from the tLRD that would resemble the tail of the Stingray. We include a cutout showing the position of the MSA slits. (2) Cutouts of $F300M - F335M$ (top) and $F410M - F430M$ (bottom) showing the Hβ+OIII and Hα emission, respectively. Bottom: Postage stamps of these sources in different NIRCam bands, not convolved to $F444W$ resolution. They are plotted following the same scale.

3.2. Revised photometry and potential LRD nature

Given the proximity of the sources and the presence of the fuzzy emission, we computed photometry in small apertures of $0.3''$ around each source, correcting for Galactic extinction, and accounting for flux losses through aperture corrections. Photometry is based on PSF-matched images homogenized to the $F444W$ resolution. We used the empirical PSFs, obtained by median-stacking non-saturated bright stars (Sarrouh et al. 2024, 2025).

Aperture corrections are based on the ratio between the flux enclosed within 2.5×$R_{\rm Kron}$ (Kron 1980) and the $0.3''$ aperture photometry in the $F200W$ band, which is not susceptible to contamination from emission lines at this redshift. Uncertainties were derived following the procedure described in Sarrouh et al. (2025), based on the flux in 2,000 apertures placed in blank regions of the sky for $0.3''$ circular apertures. In Appendix A, we also considered an additional correction to test the potential fuzz contamination in the tLRD photometry and SED derived properties. The photometric points from the tLRD, BBG, and SAT1 are displayed in Figs. 2, 3, and 4, respectively. We ran `EAzY` to derive photo-zs for all the sources, choosing the standard templates augmented with the Larson et al. (2023) set and the intergalactic medium attenuation curve of Asada et al. (2025).

C1 can only be identified in the short wavelength bands in Fig. 1, due to the image's resolution, and its proximity to the tLRD makes its study quite challenging. C2, C3, and the fuzzy structure are likely $z \sim 0.8$ projections. In Appendix B, we include the photometry and SED fitting of C1, C2, and C3. In our analysis, we will only consider the tLRD, BBG, and SAT1, for which we have spectroscopic confirmation. Table 1 shows the position of all the sources, together with their photometric and spectroscopic redshifts.

The presence of a broad Hα line in the tLRD spectrum, its blue rest-frame UV slope, and its compactness could be indicative of potential LRD activity in this galaxy. We computed the LRD photometric criteria from Kocevski et al. (2024) and Kokorev et al. (2024) and found that the rest-frame UV slope is compatible with LRD emission but the rest-frame optical slope does

Table 2: Values for the criteria established in Kokorev et al. (2024) and Kocevski et al. (2024) computed for the tLRD.

Criterion	Value
Kokorev+24	
$F115W - F150W < 0.8$ mag	0.13 mag
$F200W - F277W > 0.7$ mag	1.00 mag
$F200W - F356W > 1.0$ mag	0.36 mag
$bd : F115W - F200W > -0.5$ mag	0.24 mag
$f_{f444w}(0.5'')/f_{f444w}(0.3'') < 1.7$	1.33
Kocevski+24	
$S/N_{F444W} > 12$	249
$\beta_{\rm opt} > 0$	−1.36
$-2.8 < \beta_{\rm UV} < -0.37$	−1.59
$r_{\rm h} < 1.5 r_{\rm h,\,stars}$	1.72 pix
$\beta_{F277W-F356W} > -1$	−4.35
$\beta_{F277W-F410M} > -1$	0.26
Optical slope from spec is -0.41^*	

Notes. The Kokorev et al. (2024) compactness criterion originally refers to the ratio between the flux measured in 0.4″and 0.2″ apertures. *bd* refers to brown dwarf; $r_{\rm h}$ is the half-light radius as measured in the $F444W$ band; and $r_{\rm h,stars}$ denotes the stellar locus (as defined in Fig. 4 from Kocevski et al. 2024). In this case $1.5 r_{\rm h,\,stars} \sim 2.6$ pix. In the Kocevski et al. (2024) criteria, $\beta = \frac{0.4\,(m_1 - m_2)}{\log(\lambda_2/\lambda_1)} - 2$. Following Table 2 in that same paper, the UV filters correspond to $F115W$, $F150W$, and $F200W$, and the optical filters to $F277W$, $F356W$, and $F444W$. Even though $\beta_{\rm opt} < 0$ as derived using $F277W$ and $F444w$, $\beta_{\rm opt} = 2.1$ when using $F356W$ and $F444W$. We also include the $\beta_{\rm opt}$ value estimated directly from the spectrum.

* This is the only reliable measurement of the optical slope, given that $F277W$, $F410M$, and $F444W$ are contaminated by strong emission lines.

not reproduce the "V"-shape criteria. The optical slope derived directly from the spectrum is larger than that derived from the photometry (which is contaminated by the presence of strong emission lines in $F277W$, $F410M$, and $F444W$), but is still not enough to pass the LRD screening. We include the values computed for each criterion in Table 2. In Sec. 5.2, we discuss a possible connection between this source and LRDs, as this galaxy system could be showing us a transitional stage between a traditional AGN and an LRD.

4. Physical properties

4.1. Emission line properties

The G395M MSA 1D spectra of the tLRD, BBG, and SAT1 are displayed in Figs. 2, 3, and 4. We measured the Hβ, [OIII]$\lambda\lambda$4959, 5007, and Hα emission using the Levenberg–Marquardt nonlinear least-squares algorithm. In the case of the tLRD's Hα measurement, we selected the Trust Region Reflective algorithm, which provides bound support, fitting the different line components. The Hβ emission from this object can be fitted using a single narrow component. Figure 5 shows the fitting of the Hα profile from the tLRD source, and Table 3 includes the luminosities derived for each line and object. There is no evidence of a broad component in the Hα emission of BBG and SAT1.

The AGN bolometric luminosity can be estimated based on the fluxes of each of these lines. We can compute $L_{\rm bol}$ based on the broad Hα flux, assuming the Greene & Ho (2005) relation and the bolometric correction from Richards et al. (2006). Netzer (2019) presented a calibration based on the narrow component of Hβ and Heckman et al. (2004) used the [OIII] line to estimate $L_{\rm bol}$ based on the study of a sample of type 2 AGN. The [OIII] calibration yields the largest estimate, $L_{\rm bol} = 1.45 \pm 0.05 \times 10^{46}$ erg/s. These numbers decrease to $4.01 \pm 0.15 \times 10^{45}$ erg/s and $0.96 \pm 0.05 \times 10^{45}$ erg/s when using the Hβ and Hα lines, respectively.

The black-hole mass (M_{BH}) can be derived from the width of the Hα broad component using the empirical relation given by Reines et al. (2013). We obtained $\log M_{BH} = 7.46 \pm 0.09\, M_\odot$, which places our source above the M_{BH} vs $M_\star$ scaling relation, in line with the $4 < z < 11$ AGNs from Maiolino et al. (2024).

The Eddington ratios are 3.89±0.21 as derived from [OIII], and 1.08±0.06 and 0.26±0.02 as obtained from Hβ and Hα. This implies that, depending on the calibration, the tLRD could be emitting at sub-Eddington to super-Eddington levels. The values derived from the Hα calibration should be considered our standard reference, especially given that we cannot resolve the broad Hβ line. It is important to note that any of these narrow lines is prone to contamination from star formation (and we see [OIII] is resolved in the NIRCam imaging), which would lead to an overestimation of the ratios. Our Hα-based estimate is compatible with Eddington ratios reported for LRDs in the literature (Lin et al. 2024 and references therein).

4.2. Spectro-photometric fitting

We used `Bagpipes` (Carnall et al. 2018) to conduct a spectro-photometric fitting of the tLRD, BBG, and SAT1. This `Python` software utilizes a Bayesian inference approach and allows fitting the UV and optical emission due to an AGN accretion disk using a double power-law model. The code also implements non-parametric SFHs by using a series of piecewise constant functions in lookback time. We used the `continuity` mode, based on the Leja et al. (2019) nonparametric SFH.

All fits were performed using the Multinest sampling algorithm, and the values set for the priors of each parameter are provided in Table C.1 in Appendix C. The emission from HST filters was not considered in our analysis, given their low signal-to-noise ratio (S/N). We fitted the spectrum + photometry of the tLRD with `Bagpipes` using a composite model consisting of a stellar population plus an AGN. For BBG and SAT1, only stellar populations were set. The z was fixed to the spectroscopic values.

The AGN continuum emission was modeled as a broken power law characterized by three parameters: two spectral slopes and the continuum flux at the break point (5100 Å). The AGN line emission is included as a single Hα line. The intensity was left free and the line width was set to 1,773 km/s, as measured from the spectrum. Nebular emission was incorporated via the ionization parameter U, and we assumed a Calzetti et al. (2000) attenuation law.

Additionally, we also used the `Dense Basis` code (Iyer & Gawiser 2017, Iyer et al. 2019) to fit the photometric data of all the galaxies and compare with the `Bagpipes` output. We ran it selecting a nonparametric SFH. Stellar population synthesis models are incorporated through the Flexible Stellar Population Synthesis (`FSPS`; Conroy & Gunn 2010) `Python` module. AGN contribution at UV-to-optical wavelengths cannot be included, so the code assumes all the emission has a stellar origin. Priors are listed in Table C.1.

Figures 2, 3, and 4 show the best-fitting models from both codes overlaid on the data; Table 3 lists the values for the different physical parameters. The two codes give consistent results,

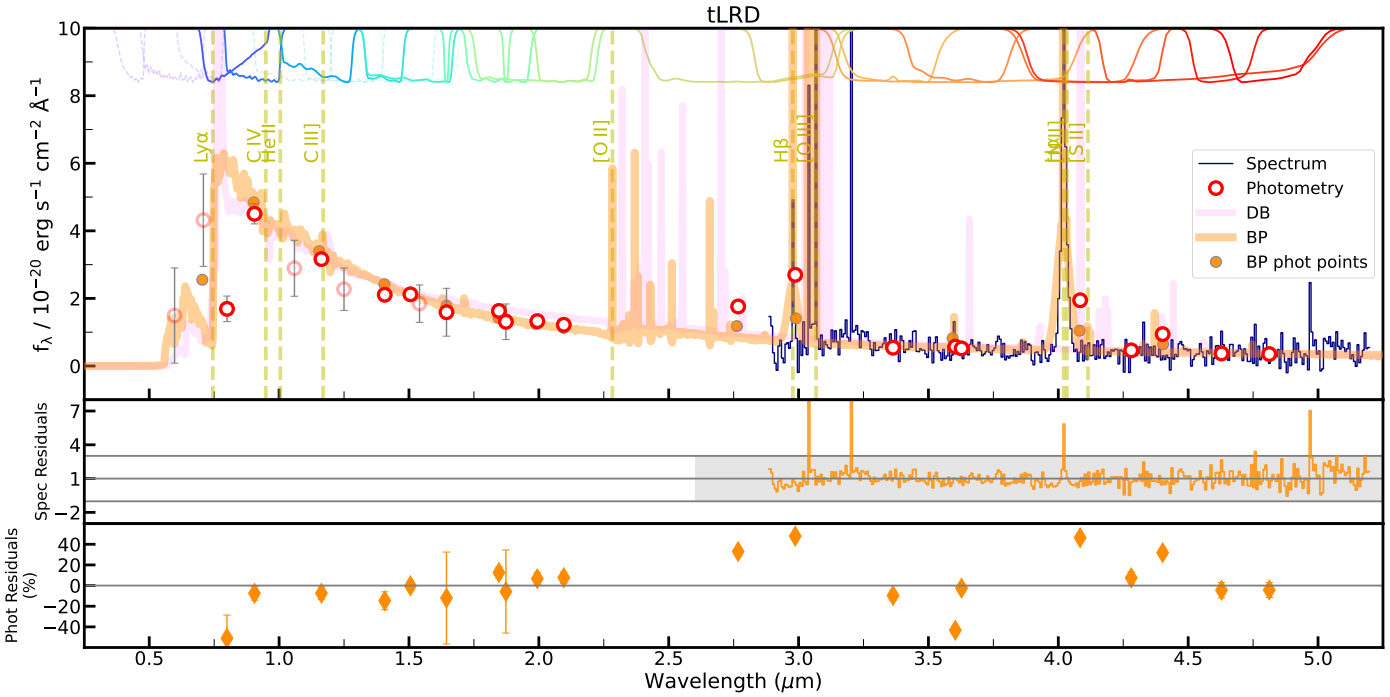

Fig. 2: G395M MSA spectra (blue) and photometry (open red circles) of the tLRD. The spectrum was rebinned in wavelength to improve S/N and readability. Lighter circles correspond to the HST photometry, which was not considered in our spectro-photometric analysis. In orange and pink, we show the best-fitting models from `Bagpipes` (spectra+photometry) and `Dense Basis` (photometry only), respectively. `Dense Basis` was allowed to explore a broader range of z, which includes the photo-z, to ensure convergence. This explains why there is a slight offset between the lines in both models. The photometric points associated with the `Bagpipes` model are shown as orange circles. We include the ACS and WFC3/HST (dashed) and NIRCam/JWST (solid) filter transmission curves at the top of the panel. Vertical dashed lines highlight the position of the main emission lines at this z. We show the `Bagpipes` residuals underneath. For the spectrum, the residuals are the ratio between the spectrum and the model. The grey shaded region corresponds to one standard deviation. For the photometry, we display the difference between the photometry and the model weighted by the photometry. Uncertainties are also depicted, representing the inverse of the S/N. The spectrum dominates the fitting in the optical, resulting in larger residuals in the photometry.

pointing to the tLRD and BBG being $\sim 10^9\,M_\odot$ sources and SAT1 being the less massive source in the group ($\sim 10^8\,M_\odot$). Even if `Dense Basis` does not consider the emission from the AGN, the $M_\star$ is only slightly overestimated with respect to the value reported by `Bagpipes`. The tLRD host is the source that shows the highest level of attenuation, with ~ 0.7 mag. Overall, the properties of this tLRD are not difficult to reconcile with traditional models, compared to those found for many LRDs (e.g., $A_v > 1-2$ mag, $M_\star > 10^{10}\,M_\odot$; see Gentile et al. 2024, Tripodi et al. 2024, Mérida et al. 2025a). In terms of their SFRs, the tLRD shows the highest value, followed by the BBG, and lastly SAT1. These values, together with the SFHs (see Sec. 4.3), reflect the star-forming nature of the system, as also suggested by the presence of emission lines in their spectra.

We also derived the AGN model from the best-fitting composite `Bagpipes` template, which is displayed in Fig. 6. The median parameters defining the broken power law correspond to $\alpha_\lambda = -1.43$, $\beta_\lambda = 0.64$, `hanorm` $= 2.24 \times 10^{-17}$ erg/s/cm^2, and $f_{5100} = 3.72 \times 10^{-21}$ erg/s/cm^2/Hz. α_λ and β_λ are the slopes on either side of 5100Å. The α_λ slope for this AGN is consistent with the slopes found for Sloan Digital Sky Survey (SDSS) quasars (Vanden Berk et al. 2001), spanning $0.044 \leq z \leq 4.789$. The continuum is normalized at 5100Å using the f_{5100} parameter, and `hanorm` sets the total flux of the Hα line.

The photometric points associated with this AGN model are also depicted, as well as the photometry of the stellar component, which was estimated by subtracting the AGN photometry from the observed photometry. This approach assumes that any remaining emission can only be powered by stars. According to `Bagpipes`, the rest-frame UV photometry is a composite of stellar and AGN emission, with $\sim 56\%$ being supplied by the AGN. Optical emission would be primarily driven by the AGN, although there is likely a significant contribution from stars powering [OIII] + Hβ (see Appendix D). A red stellar component, outshone by the AGN, may also contribute to the optical (Narayanan et al. 2024, Whitler et al. 2023).

4.3. Star formation histories

The SFHs of the three galaxies, obtained with `Bagpipes` and `Dense Basis` using a nonparametric approach (see Sec. 4.2), are displayed in Fig. 7. The two codes provide consistent results, showing that all three galaxies are star-forming at $z = 5.12$.

This figure also shows that the tLRD and SAT1's SFH are very similar in shape, with a different scaling factor; tLRD presents higher SFRs. They display a rising SFH, which became steeper ~ 10 Myr prior to observation. On the other hand, the BBG shows a more complex SFH according to `Dense Basis`, with a continuous star formation until ~ 250 Myr ago, when the galaxy's SFR started following a rising trend. According to the two codes, this galaxy reached an SFR peak after which the SFH flattened. This flattening could lead to a quenching event (as the

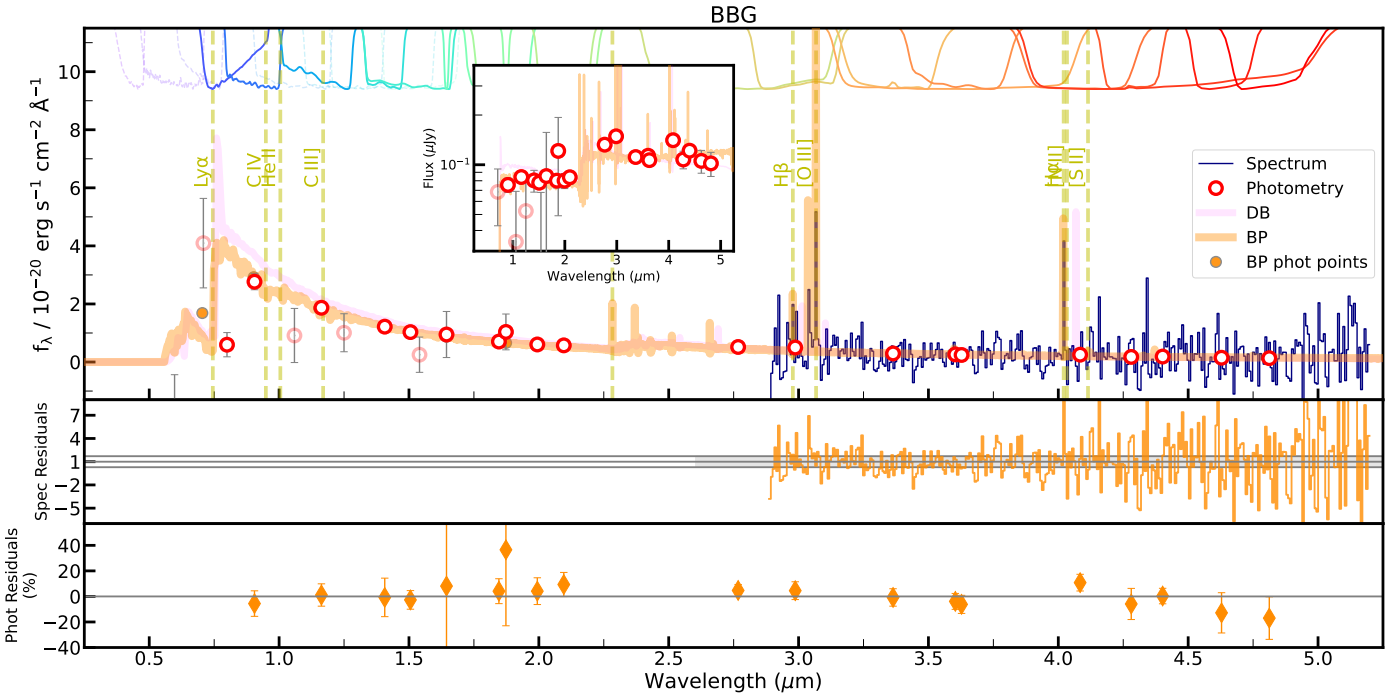

Fig. 3: G395M MSA spectra (blue) and photometry (open red circles) of the BBG. We include an inset with the photometry expressed in μJy where it is easier to spot the presence of the Balmer break. See Fig. 2 for a complete description of the markers and color codes used in this plot.

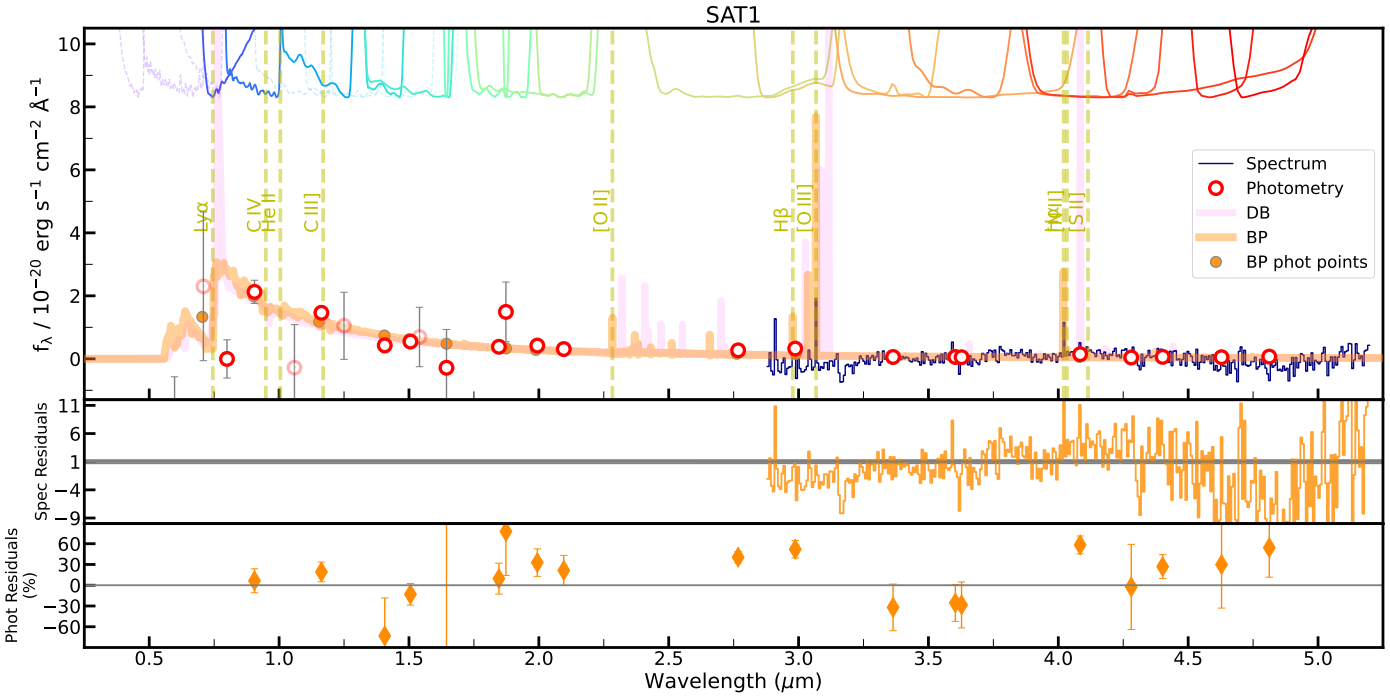

Fig. 4: G395M MSA spectra (blue) and photometry (open red circles) of SAT1. See Fig. 2 fo a complete description of the markers and color codes used in this plot.

quenching reported for the $z = 5.20$ BBG of Strait et al. 2023) or else the BBG's SFH could revert to a continuous or steeper trend again. In Sec. 5.1, we further analyze these trajectories in order to understand the role played by the interaction in the evolution of these galaxies.

5. Discussion

5.1. Mass growth induced by the interaction

In this $z_{spec} = 5.12$ galaxy system we see three components that display rising SFHs during part of their evolution, as well as signs of ongoing star formation. SAT1 is lower in mass, whereas

Table 3: Best-fitting parameters derived using `Bagpipes` (spectrum+photometry) and `Dense Basis` (photometry only).

ID	log $M_\star/M_\odot$	log SFR [$M_\odot$/yr]	A_v [mag]	log $M_\star/M_\odot$	log SFR [$M_\odot$/yr]	A_v [mag]	$L_{H\alpha}$	$L_{H\beta}$	$L_{[OIII]\lambda4959}$	$L_{[OIII]\lambda5007}$
	Bagpipes			**Dense Basis**			[10^{41} erg/s]			
tLRD	$9.08^{9.14}_{9.03}$	$1.09^{1.15}_{1.04}$	$0.72^{0.80}_{0.63}$	$9.25^{9.25}_{9.25}$	$1.14^{1.17}_{1.16}$	$0.82^{0.83}_{0.82}$	82.78±1.86 B:54.52±1.69 N:28.26±1.07	7.93±0.85	13.20±0.85	41.47±1.32
BBG	$9.02^{9.09}_{8.95}$	$0.73^{0.83}_{0.61}$	$0.28^{0.40}_{0.14}$	$9.10^{9.22}_{8.94}$	$0.52^{0.89}_{0.45}$	$0.03^{0.09}_{0.02}$	8.14±0.98	< 3.26	3.58±0.81	9.97±1.06
SAT1	$7.84^{8.02}_{7.66}$	$-0.27^{0.13}_{-0.35}$	$0.07^{0.13}_{0.03}$	$8.28^{8.60}_{8.06}$	$0.10^{0.22}_{-0.02}$	$0.11^{0.23}_{0.03}$	2.19±0.36	< 1.15	1.43±0.31	4.24±0.40

Notes. We include the 16th and 84th percentiles as upper and lower bounds for the SED-derived properties. The star formation rates correspond to SFR_{100}. `Dense Basis` assumes all the emission comes from stars, whereas `Bagpipes` includes AGN emission in the fit. In column 8, B and N denote broad and narrow components, respectively. The width of the H_α line is 1,773 km/s. The BBG and SAT1 Hβ emission line measurements are 2σ upper limits.

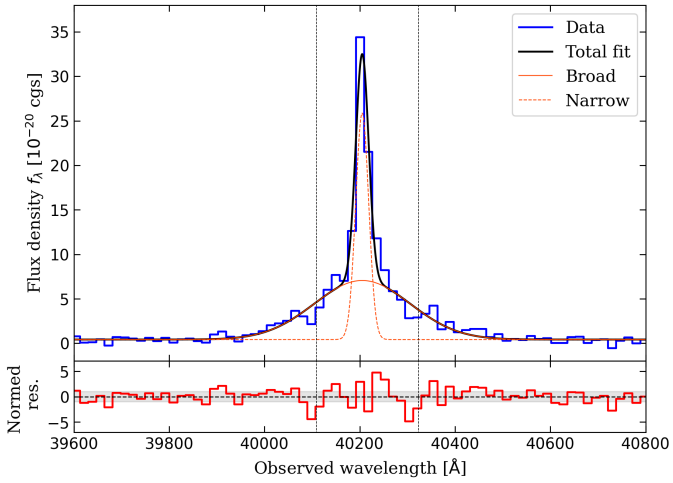

Fig. 5: Hα fit (black line) for the tLRD compared to the data (blue). The spectrum was rebinned in wavelength to improve S/N and readability. The solid (dashed) red line shows the fit to the broad (narrow) component. The normed residuals (spectrum − model, normalized by the error) are displayed underneath. The shaded gray region corresponds to $\pm1\sigma$.

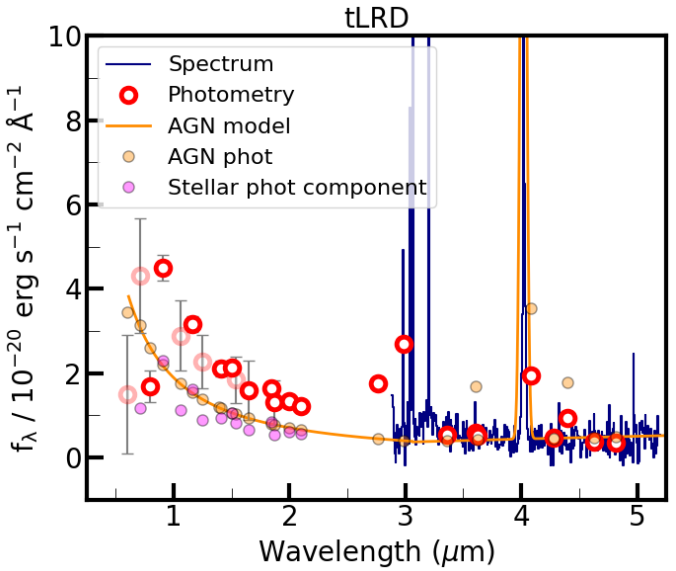

Fig. 6: Spectrum (blue) and photometry (open red circles) of the tLRD source, together with the AGN model extracted from `Bagpipes` (orange). The photometric points associated with the model are shown as orange circles. The photometry linked to the stellar component, which we obtain by subtracting the AGN model photometry from the observed photometry, is displayed as fuchsia circles. In the optical, the photometry from the AGN model lies above the photometry and the photometric points derived from the spectrum.

the other two sources have currently comparable $M_\star$ of $10^9\,M_\odot$. One of these galaxies hosts an AGN, and the other shows a Balmer break. The three objects are close together on the sky and at the same z. Considering 10 kpc for the scale of the system (see Fig. 1) and assuming a relative velocity of 100 km/s (Lambas et al. 2003, Ellison et al. 2011), the crossing time would be ∼ 100 Myr for this group. This estimate is consistent with the key timescales evidenced by the SFHs (see Fig. 7), suggesting that interactions between the three galaxies could play a role in their star formation histories. We aim to check whether the galaxies' growth could be attributed to secular processes or else was driven by environmental effects.

To examine how the galaxies in the Stingray system evolved, we first estimated their mass assembly histories. Figure 8 shows the mass growth of tLRD, BBG, and SAT1, derived by integrating their `Bagpipes` SFHs, while assuming a return fraction of 0.3 (i.e., that expected for a Chabrier 2003 IMF). ∼ 500 Myr ago BBG was the most massive source, with $M_\star = 10^{8.2}\,M_\odot$. tLRD's mass was $10^{7.4}\,M_\odot$ while SAT1 was the least massive object, with $10^{6.7}\,M_\odot$. BBG increased its $M_\star$ by ∼ 0.8 dex during the last 500 Myr, while tLRD's mass grew ∼ 1.5 dex and SAT1's mass ∼ 1 dex. tLRD and SAT1 assembled a larger fraction of their $M_\star$ than BBG during the same 500 Myr period. This is especially the case for tLRD, which showed a significant steepening of its mass growth ∼ 100 Myr ago.

To understand whether these differences in the mass growth can be due to the impact of interactions, as well as to the presence of an AGN in tLRD, we compared the observed mass growth to that of hypothetical sources that evolved along the star-forming main sequence (MS). By comparing the fiducial MS galaxies with our observations, we can infer whether the growth observed in our three galaxies could be attributed to secular processes or if a contribution from other factors should be claimed. To calculate the histories of the reference MS galaxies, we took the starting $M_\star$ of our three objects at $t = 500$ Myr as the seed mass. We

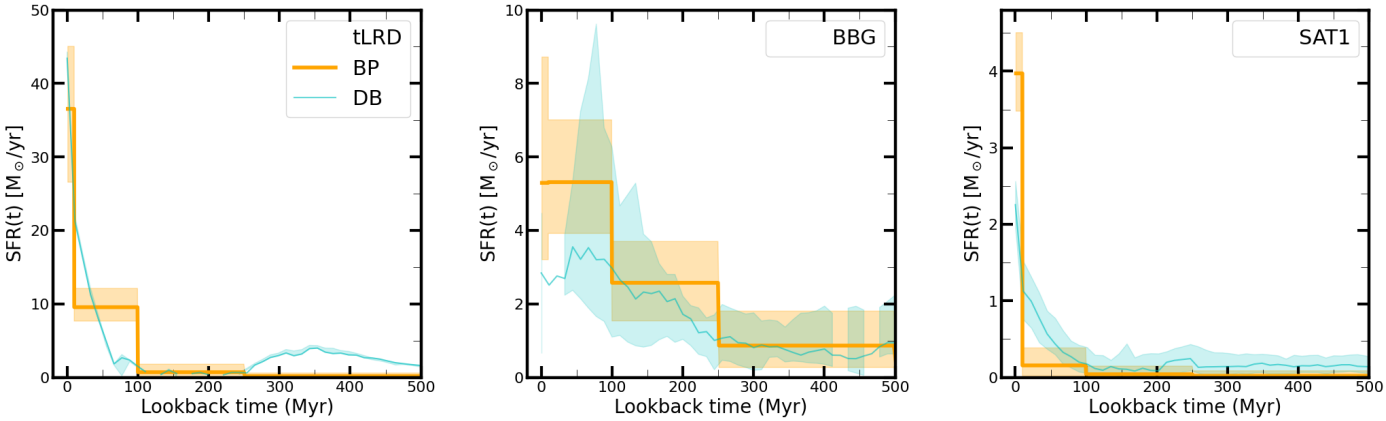

Fig. 7: Star formation histories of the tLRD (left), BBG (middle), and SAT1 (right), obtained using `Bagpipes` (orange), based on the Leja et al. (2019) approach, and `Dense Basis` (cyan). The shaded regions correspond to the area enclosed within the 16th and 84th percentiles.

then evolved them over time, using the parameters from the MS relation provided in Mérida et al. (2025b) for $5 < z \leq 7$ galaxies.

The results of this comparison are as follows. The BBG mass assembly history is consistent with evolution along the MS, while tLRD's final mass is $\sim$ 0.7 dex higher than that expected for an MS galaxy. tLRD started deviating from the MS trend 100 Myr ago. The growth of SAT1 is more difficult to interpret. This was a very low-$M_\star$ source that could be in a latent or lulling phase 500 Myr ago (see Looser et al. 2024, Mintz et al. 2025). However, a potential latent state in SAT1 cannot be confirmed since MS studies at this z are not complete down to these low $M_\star$, preventing us from modeling SAT1's reference MS galaxy with confidence. We note, however, that the final mass of SAT1 is roughly consistent with that of an MS galaxy, considering its $M_\star$ at $t = 500$ Myr.

Figure 8 also depicts the SFHs of the sources, alongside the SFHs of the model reference MS galaxies. Shown with dotted curves, we also include hypothetical SFHs of three objects that follow the same mass assembly histories as our galaxies; in other words, the seed mass is reset to the $M_\star$ achieved in each time bin, rather than being set once at 500 Myr. BBG displays several upturns in its SFH, but they are all consistent with evolution on the MS (especially if we take into account the typical MS scatter of $\sim$ 0.2 dex at this z). tLRD's SFH is consistent with the MS tracking up to $\sim$ 100 Myr ago, when it experienced a star formation upturn that displaced it $\sim$ 1 dex above the MS. 10 Myr ago, tLRD experienced a new upturn that elevated it 1.5 dex above the MS, or 1 dex if we restart the MS at $t = 100$ Myr. The combination of these two bursts allowed tLRD to equalize BBG in $M_\star$. SAT1's SFH falls slightly below the MS at early times, although it is consistent with it within the SFH uncertainties. Its subsequent evolution is also consistent with the MS within uncertainties up to 10 Myr ago, when the galaxy experienced an upturn that moved it $\sim$ 1.5 dex above the MS.

In summary, BBG's evolution can be explained by secular evolution on the MS. During this time, it developed a Balmer break, while stars continued forming within this galaxy, but at a rate that's consistent with that expected of an MS galaxy. BBG is not bursting, as also reflected by the strength of its emission lines versus that of the UV continuum. In contrast to BBG, tLRD experienced two bursts of star formation that cannot be explained by evolution on the MS. These happened 10 Myr and 100 Myr ago. Lastly, SAT1's evolution is also consistent with the MS except for a recent burst of star formation that started 10 Myr ago. Although starbursts can have origins other than interactions, the proximity of these sources makes the environment a likely precursor of these events.

Given the configuration of all three galaxies at the time of the observation and the estimated crossing times, we propose a scenario in which tLRD encountered BBG 100 Myr ago. This interaction boosted mainly the star formation in tLRD, which was the less massive source by 0.6 dex – or a factor of 4 – in mass at that time. BBG might also have experienced some increase in its star formation as a result of the encounter, but this was not enough to push the galaxy into a starburst phase. 10 Myr ago, SAT1 joined the system, interacting with BBG, which is closer in projected distance. Again, this effect was more noticeable in SAT1, given its $M_\star$ that is 1.5 dex – or $\sim$30 times lower – than the masses of the other two galaxies. The 10 Myr upturn in tLRD could be attributed to an interaction with SAT1, although 10 Myr ago tLRD's $M_\star$ was already comparable to that of BBG, and it is located further away from SAT1.

Alternatively, this 10 Myr burst in tLRD could be due to feedback from its AGN. AGN activation can be delayed with respect to star formation triggering (see Emonts et al. 2006, Omori et al. 2025, O'Ryan et al. 2025). AGN luminosities in realistic hydrodynamic models do not peak at the same time as the gas density on small scales, but rather at somewhat later times, when most of the gas has been consumed by star formation and/or expelled by stellar feedback (Hopkins 2012). Gravitational torques, which govern further inflow into the center, are relatively inefficient in gas-dominated systems. However, stars provide an efficient angular momentum sink, allowing for a more rapid inflow (Hopkins 2012). This can result in a delay of $\sim$ 100 Myr between the star formation and the AGN activations. The delayed AGN triggering can be a consequence of the 100 Myr burst induced in the tLRD–BBG's encounter. AGN feedback would be the mechanism responsible for triggering a new star formation upturn in tLRD $\sim$ 10 Myr ago.

We acknowledge that this discussion is based on the assumption that the SED-derived properties of these galaxies, especially the SFHs, are reliable. This assumption is particularly important in tLRD. Although it can be well fitted with `Bagpipes`, it exhibits LRD features, which are a challenge for current models. To ensure the consistency of our results, we tested changing the AGN component priors to force alternative solutions. We then checked the impact on the SFHs. These results are included in

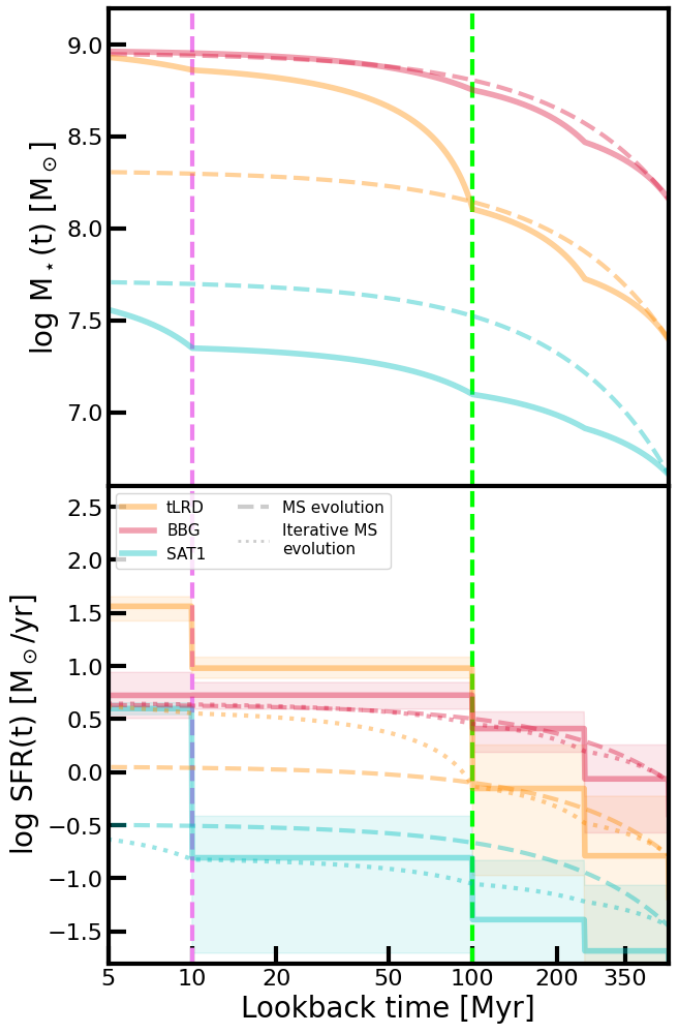

Fig. 8: Top: mass assembly histories of tLRD (solid orange), BBG (solid red), and SAT1 (solid cyan) on log scale. We also show the mass growth of these galaxies, assuming that they followed the main sequence (dashed lines, in the same color code). To calculate these MS tracks, we used the main sequence fit from Mérida et al. (2025b) at $5 < z \leq 7$ and the $M_\star$ of the sources at $t = 500$ Myr. We assumed a return fraction of 0.3. Vertical lines highlight $t = 10$ Myr (violet) and $t = 100$ Myr (lime), respectively. Bottom: SFHs of our sources, following the same color code. SFHs of analogous galaxies evolving along the main sequence since $t = 500$ Myr ago are also depicted. Additionally, we show the MS evolution resetting this seed mass to that achieved in each time bin (dotted lines). The shaded region shows the SFH uncertainty of each source. Additionally, we should take into account the main sequence scatter, which is ~ 0.2 dex at this z.

Appendix D. There, we demonstrate that trends persist despite changes in the AGN priors.

Finally, it is worth noting the broader connection of the Stingray system to the emerging picture of enhanced hierarchical galaxy formation at high z. This group resembles the Building Blocks System (BBS) discussed in Asada et al. (in prep). It consists of a BBG and two low-mass star-forming galaxies at $z = 5.2$, and is likely destined to evolve into a Milky-Way-mass galaxy by the present day. BBS is in the process of "boosted hierarchical assembly", whereby the $M_\star$ of the resulting merger product is not just the sum of the pre-existing masses of the individual components, but is also dramatically boosted by the interaction-induced bursts of star formation. In the case of the Stingray's tLRD, $M_\star$ appears to have been boosted fourfold by the interaction prior to the likely future merger with BBG.

Although more massive than BBS, our galaxy system provides another key piece to the boosted hierarchical assembly scenario, which is AGN activity. The latter can potentially enhance the effects of the environment, extending the interaction-induced star formation burst as a result of a delayed AGN activation. This can lead to an even more rapid mass assembly in these galaxies. Moreover, we see that the environment can act as a precursor of black hole mass growth in low-$M_\star$ high-z objects.

5.2. Transitional LRDs

The AGN in the Stingray shows properties that are compatible with an LRD phase. It is compact and blue in the rest-frame UV (see Sec. 3.2) and shows a broad Hα component (Sec. 4.1). However, the optical emission does not pass the LRD screenings. Its AGN is likely emitting in the sub-Eddington regime (Sec. 4.1), in line with LRDs reported in previous works.

In Fig. 9, we compared the properties of this AGN with the LRDs from Hviding et al. (2025), extracted from the Red Unknowns: Bright Infrared Extragalactic Survey (RUBIES; de Graaff et al. 2025a). These objects display a spectroscopic "V"-shaped continuum, compact sizes, and broad Balmer lines. The figure is adapted from Figs. 6 and 8 in Hviding et al. (2025). The first panel shows the position of our source in the $\beta_{\rm opt}$–$\beta_{\rm UV}$ plane. The combination of the spectrum and the photometry places our AGN in the intersection between the LRD population and the $z_{\rm spec} > 3.1$ RUBIES galaxies. The $\beta_{\rm opt} - \beta_{\rm UV}$ plane was also explored in Hainline et al. (2025) (see Fig. 4 in that paper). Near the UV and optical slope values of tLRD, we see a fraction of Type 1 AGNs from Juodžbalis et al. (2025), one Type 1 AGN from Matthee et al. (2024), and one Type II AGN from Mazzolari et al. (2025). There is a significant fraction of high-z AGNs, mainly Type II, that exhibit much bluer $\beta_{\rm opt}$. Most Type I AGNs are located within the LRD locus. This could suggest that Type I AGNs are mostly compatible with LRDs or similar sources to tLRD. However, Hainline et al. (2025) pointed out that LRDs are easy to select (they are more luminous) and thus easy to follow-up spectroscopically. So far, Type I AGN at $z > 6$ are mostly consistent with LRDs, as a result of the difficulty in selecting normal Type I AGNs at these redshifts.

In the second panel, we show the position of our source in the $M_{\rm UV} - L_{\rm H\alpha}$ plane, compatible with the LRD locus instead of the broadline sources locus. Considering these and the properties previously reported, it is possible that this object was caught in a transition phase bridging normal AGNs and LRDs. In other words, at some point an LRD evolves with z into a different state that no longer meets the selection criteria, which means there must be a transition phase in which these galaxies still exhibit LRD features while simultaneously developing new characteristics (Billand et al. 2025). The question that arises is whether this tLRD is evolving into a regular LRD or if the LRD phase is fading out instead.

Billand et al. (2025) investigated the possible evolution of LRDs by identifying candidates in the Cosmic Evolution Early Release Science data (CEERS; Finkelstein et al. 2017, Finkelstein et al. 2025) that could represent the descendants of LRDs. They affirmed that the decline in the number density of LRDs with cosmic time is driven by the acquisition of a stellar component that settles in the galaxy's outskirts. As $M_\star$ grows, the char-

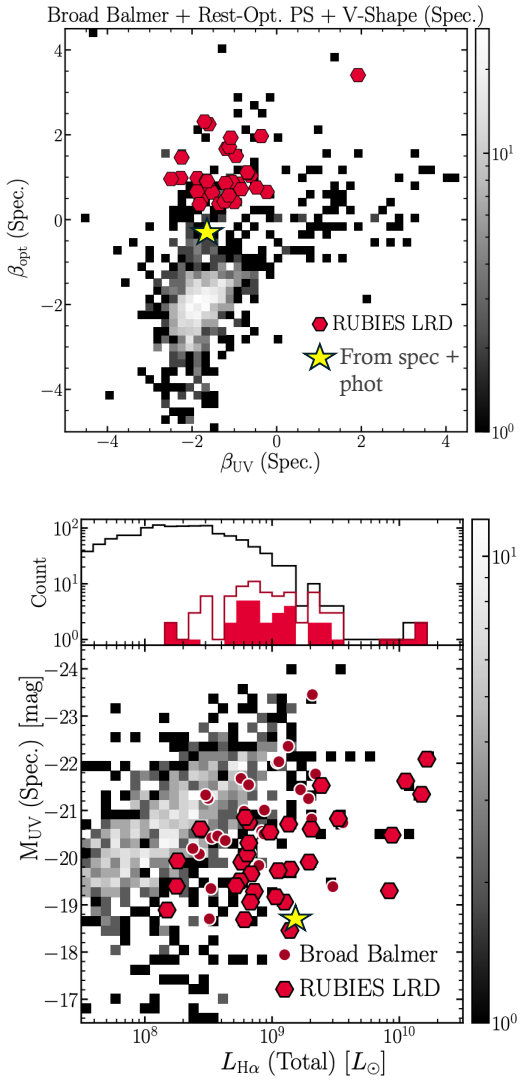

Fig. 9: Adapted version of Figs. 6 and 8 from Hviding et al. (2025) showing β_{opt} vs. β_{UV} (top) and M_{UV} vs. $L_{H\alpha}$ (bottom) of our source (yellow star) with respect to the LRDs selected in RUBIES (red hexagons); these sources show broad lines, are unresolved, and display "V"-shaped features. They include $z_{spec} > 3.1$ galaxies from RUBIES as 2D grayscale histograms. Sources with broad Balmer lines are depicted as red circles. In the bottom panel, $L_{H\alpha}$ was derived from the spectrum (see Table 3) while M_{UV} was estimated from the `Bagpipes` best-fitting model.

acteristic "V"-shape fades and the physical size of the galaxies increases. Similarly, Hainline et al. (2025) proposed a trend between luminosity and optical slope, according to which lower-luminosity AGNs display bluer slopes as a consequence of the star-forming host galaxy becoming more dominant in such weak AGNs.

Billand et al. (2025) proposed several scenarios, including mergers, for the LRD−traditional AGN transition. However, their findings point to cold accretion as the leading mechanism. In that work, galaxies were selected to keep a red optical core. They display rest-frame UV slopes that do not meet the "V"-shape criteria, as well as sizes not compatible with being compact, unlike tLRD.

A different scenario for this transition was proposed by Kido et al. (2025) within the BH* framework. They affirmed that a decrease in the infalling mass onto the BH envelope can lead to a decrease in its mass (i.e., when the infall rate is lower than the Eddington accretion rate). Together with BH mass growth, this leads to the dissolution of the gas envelope. According to Inayoshi et al. (2025a), supernova explosions from massive stars in nuclear starbursts can inject energy and momentum that is able to expel gas from the nucleus, quenching gas supply to the BH envelope, and ultimately driving a transition into normal AGN phases. The LRD stage would only persist for one-third of a Salpeter time. This scenario could explain the features we see in tLRD, which no longer exhibits a red optical slope.

The existence of channels for LRD disruption suggests the presence of inverse channels as well. For instance, a potential gas envelope can develop as a result of super-Eddington accretion; if this were to happen, the mass infall rate from the interstellar medium must be significantly larger than the BH's Eddington rate. Otherwise, radiative and mechanical feedback from the BH will suppress the infall (Kido et al. 2025).

The LRD state could be a phase that can be activated and deactivated (although above a certain critical M_{BH}, subsequent LRD phases are not very likely; Inayoshi et al. 2025a), probably linked to the AGN's level of accretion, directly related to the burstiness of the system. The environment can play a key role in both activating and deactivating the LRD phase, as in our galaxy system (see also Mérida et al. 2025a). Within a certain cosmic time window, the Universe's environmental conditions facilitate the emergence of LRDs, while at lower z this channel becomes increasingly compromised.

Whether tLRD will move towards a more traditional AGN or else will evolve into a regular LRD is something we cannot clarify until we understand the nature of these objects. According to our results, this transition phase (regardless of its direction) could be linked to an environmental process that began $\sim$ 100 Myr ago, although the conditions of this system are very particular. To fully understand the LRD phase and its ruling mechanisms, it will be crucial to study a larger and more complete sample of these transitional objects, which exhibit mixed features of LRDs and normal AGNs.

6. Summary and conclusions

In this work, we present *The Stingray*: a galaxy system at $z_{spec} = 5.12$ found in an overdensity in the MACS 1149 flanking field within the CANUCS observations. We analyzed the properties of 3 galaxies in this system, dubbed tLRD, BBG, and SAT1, which show up as an interacting system. Similar to the Building Blocks System of Asada et al. (in prep.), it reflects an example of a "boosted hierarchical galaxy assembly" process.

tLRD and SAT1's SFHs show evidence of interaction processes that took place 10 and 100 Myr ago, linked to BBG. The result of these interactions led to a more rapid growth of their stellar mass than that driven by secular processes, which are dominant in BBG. Additionally, tLRD's burst 10 Myr ago can be attributed to a delay in the activation of the AGN activity relative to the star formation burst. A later activation could extend the interaction-driven burst that took place in tLRD 100 Myr ago. Thus, the environment allows for black hole mass growth in such low-$M_\star$ high-z systems.

The AGN in the Stingray shows properties that are partially compatible with LRDs. tLRD could thus be a transition object (see Billand et al. 2025) showing us the emergence or fading out

of an LRD phase at $z_{\rm spec} = 5.12$, with galaxy-galaxy interactions being a potential trigger.

Acknowledgements. This research was enabled by grant 18JWST-GTO1 from the Canadian Space Agency and Discovery Grant and Discovery Accelerator funding from the Natural Sciences and Engineering Research Council (NSERC) of Canada to MS.
This research used the Canadian Advanced Network For Astronomy Research (CANFAR) platform operated in partnership by the Canadian Astronomy Data Centre and The Digital Research Alliance of Canada with support from the National Research Council of Canada, the Canadian Space Agency, CANARIE, and the Canada Foundation for Innovation.
This work is based on observations made with the NASA/ESA/CSA James Webb Space Telescope. The data were obtained from the Mikulski Archive for Space Telescopes at the Space Telescope Science Institute, which is operated by the Association of Universities for Research in Astronomy, Inc., under NASA contract NAS 5-03127 for JWST. JWST observations are associated with programs JWST-GTO-1208, -4527, and GO-3362.

References

Ananna , T. T., Bogdán, Á., Kovács, O. E., Natarajan, P., & Hickox, R. C. 2024, ApJ, 969, L18
Asada, Y., Desprez, G., Willott, C. J., et al. 2025, ApJ, 983, L2
Barro, G., Pérez-González, P. G., Kocevski, D. D., et al. 2024, ApJ, 963, 128
Bertin, E. & Arnouts, S. 1996, A&AS, 117, 393
Billand, J.-B., Elbaz, D., Gentile, F., et al. 2025, arXiv e-prints, arXiv:2507.04011
Brammer, G. 2022, gbrammer/msaexp: Full working version with 2d drizzling and extraction
Brammer, G. 2023, grizli
Brammer, G. B., van Dokkum, P. G., & Coppi, P. 2008, ApJ, 686, 1503
Calzetti, D., Armus, L., Bohlin, R. C., et al. 2000, ApJ, 533, 682
Cappellari, M. & Copin, Y. 2003, MNRAS, 342, 345
Carnall, A. C., McLure, R. J., Dunlop, J. S., & Davé, R. 2018, MNRAS, 480, 4379
Chabrier, G. 2003, PASP, 115, 763
Chen, C.-H., Ho, L. C., Li, R., & Inayoshi, K. 2025, ApJ, 989, L12
Conroy, C. & Gunn, J. E. 2010, FSPS: Flexible Stellar Population Synthesis, Astrophysics Source Code Library, record ascl:1010.043
de Graaff, A., Brammer, G., Weibel, A., et al. 2025a, A&A, 697, A189
de Graaff, A., Rix, H.-W., Naidu, R. P., et al. 2025b, arXiv e-prints, arXiv:2503.16600, submitted to A&A
Doyon, R., Willott, C. J., Hutchings, J. B., et al. 2023, PASP, 135, 098001
Ellison, S. L., Patton, D. R., Mendel, J. T., & Scudder, J. M. 2011, MNRAS, 418, 2043
Emonts, B. H. C., Morganti, R., Tadhunter, C. N., et al. 2006, A&A, 454, 125
Finkelstein, S. L., Bagley, M. B., Arrabal Haro, P., et al. 2025, ApJ, 983, L4
Finkelstein, S. L., Dickinson, M., Ferguson, H. C., et al. 2017, The Cosmic Evolution Early Release Science (CEERS) Survey, JWST Proposal ID 1345. Cycle 0 Early Release Science
Gardner, J. P., Mather, J. C., Abbott, R., et al. 2023, PASP, 135, 068001
Gentile, F., Casey, C. M., Akins, H. B., et al. 2024, ApJ, 973, L2
Greene, J. E. & Ho, L. C. 2005, ApJ, 630, 122
Greene, J. E., Labbe, I., Goulding, A. D., et al. 2024, ApJ, 964, 39
Hainline, K. N., Maiolino, R., Juodžbalis, I., et al. 2025, ApJ, 979, 138
Heckman, T. M., Kauffmann, G., Brinchmann, J., et al. 2004, ApJ, 613, 109
Heintz, K. E., Brammer, G. B., Watson, D., et al. 2025, A&A, 693, A60
Hopkins, P. F. 2012, MNRAS, 420, L8
Hviding, R. E., de Graaff, A., Miller, T. B., et al. 2025, arXiv e-prints, arXiv:2506.05459
Inayoshi, K. 2025, ApJ, 988, L22
Inayoshi, K. & Maiolino, R. 2025, ApJ, 980, L27
Inayoshi, K., Murase, K., & Kashiyama, K. 2025a, arXiv e-prints, arXiv:2509.19422
Inayoshi, K., Shangguan, J., Chen, X., Ho, L. C., & Haiman, Z. 2025b, arXiv e-prints, arXiv:2505.05322
Iyer, K. & Gawiser, E. 2017, ApJ, 838, 127
Iyer, K. G., Gawiser, E., Faber, S. M., et al. 2019, ApJ, 879, 116
Jakobsen, P., Ferruit, P., Alves de Oliveira, C., et al. 2022, A&A, 661, A80
Ji, X., Maiolino, R., Übler, H., et al. 2025, arXiv e-prints, arXiv:2501.13082, submitted to MNRAS
Juodžbalis, I., Maiolino, R., Baker, W. M., et al. 2025, arXiv e-prints, arXiv:2504.03551
Kido, D., Ioka, K., Hotokezaka, K., Inayoshi, K., & Irwin, C. M. 2025, arXiv e-prints, arXiv:2505.06965
Kocevski, D. D., Finkelstein, S. L., Barro, G., et al. 2024, arXiv e-prints, arXiv:2404.03576, accepted for publication in ApJ
Kocevski, D. D., Finkelstein, S. L., Barro, G., et al. 2025, ApJ, 986, 126
Kokorev, V., Caputi, K. I., Greene, J. E., et al. 2024, ApJ, 968, 38
Kron, R. G. 1980, ApJS, 43, 305
Labbe, I., Greene, J. E., Matthee, J., et al. 2024, arXiv e-prints, arXiv:2412.04557
Labbé, I., van Dokkum, P., Nelson, E., et al. 2023, Nature, 616, 266
Lambas, D. G., Tissera, P. B., Alonso, M. S., & Coldwell, G. 2003, MNRAS, 346, 1189
Larson, R. L., Hutchison, T. A., Bagley, M., et al. 2023, ApJ, 958, 141
Leja, J., Carnall, A. C., Johnson, B. D., Conroy, C., & Speagle, J. S. 2019, ApJ, 876, 3
Lin, X., Fan, X., Cai, Z., et al. 2025, arXiv e-prints, arXiv:2507.10659
Lin, X., Wang, F., Fan, X., et al. 2024, ApJ, 974, 147
Looser, T. J., D'Eugenio, F., Maiolino, R., et al. 2024, Nature, 629, 53
Ma, Y., Greene, J. E., Setton, D. J., et al. 2025, arXiv e-prints, arXiv:2504.08032
Maiolino, R., Scholtz, J., Curtis-Lake, E., et al. 2024, A&A, 691, A145
Matthee , J., Naidu, R. P., Brammer, G., et al. 2024, ApJ, 963, 129
Mazzolari, G., Scholtz, J., Maiolino, R., et al. 2025, A&A, 700, A12
Mérida, R. M., Gaspar, G., Sawicki, M., et al. 2025a, A&A, 698, A317
Mérida, R. M., Sawicki, M., Iyer, K. G., et al. 2025b, arXiv e-prints, arXiv:2509.22871
Mintz, A., Setton, D. J., Greene, J. E., et al. 2025, arXiv e-prints, arXiv:2506.16510
Naidu, R. P., Matthee, J., Katz, H., et al. 2025, arXiv e-prints, arXiv:2503.16596, submitted
Narayanan, D., Lower, S., Torrey, P., et al. 2024, ApJ, 961, 73
Netzer, H. 2019, MNRAS, 488, 5185
Oke, J. B. & Gunn, J. E. 1983, ApJ, 266, 713
Omori, K. C., Bottrell, C., Bellstedt, S., et al. 2025, ApJ, 989, 73
O'Ryan, D., Simmons, B. D., Faisst, A. L., et al. 2025, MNRAS, 539, 2967
Pérez-González, P. G., Barro, G., Rieke, G. H., et al. 2024, ApJ, 968, 4
Reines, A. E., Greene, J. E., & Geha, M. 2013, ApJ, 775, 116
Richards, G. T., Lacy, M., Storrie-Lombardi, L. J., et al. 2006, ApJS, 166, 470
Rieke, M. J., Kelly, D. M., Misselt, K., et al. 2023, PASP, 135, 028001
Rinaldi, P., Bonaventura, N., Rieke, G. H., et al. 2024, arXiv e-prints, arXiv:2411.14383
Rusakov, V., Watson, D., Nikopoulos, G. P., et al. 2025, arXiv e-prints, arXiv:2503.16595, submitted to Nature
Sarrouh, G. T. E., Asada, Y., Martis, N. S., et al. 2025, arXiv e-prints, arXiv:2506.21685
Sarrouh, G. T. E., Muzzin, A., Iyer, K. G., et al. 2024, ApJ, 967, L17
Setton, D. J., Greene, J. E., Spilker, J. S., et al. 2025, ApJ, 991, L10
Strait, V., Brammer, G., Muzzin, A., et al. 2023, ApJ, 949, L23
Tanaka, T. S., Silverman, J. D., Shimasaku, K., et al. 2024, arXiv e-prints, arXiv:2412.14246, submitted to PASJ
Tripodi, R., Martis, N., Markov, V., et al. 2024, arXiv e-prints, arXiv:2412.04983, submitted to Nature Communications
Vanden Berk, D. E., Richards, G. T., Bauer, A., et al. 2001, AJ, 122, 549
Whitler, L., Stark, D. P., Endsley, R., et al. 2023, MNRAS, 519, 5859
Willott, C. J., Doyon, R., Albert, L., et al. 2022, PASP, 134, 025002
Zhang, Z., Jiang, L., Liu, W., & Ho, L. C. 2024, arXiv e-prints, arXiv:2411.02729, accepted for publication in ApJ
Zhuang, M.-Y., Li, J., Shen, Y., et al. 2025, arXiv e-prints, arXiv:2505.20393

Appendix A: The fuzz

Centered around C2, and covering C1, C3, and partially the tLRD, we can see a fuzzy structure that could potentially affect the measurements of all these galaxies. In this appendix, we discuss the properties of this fuzzy emission and include a correction intended to remove potential contamination in the tLRD photometry that might not be accounted for by the aperture correction.

To define this fuzzy structure, we measured its emission in residual images computed for each band. These residual images were obtained using the PSF photometry functions from `photutils`. We modeled the emission of the sources in the system with `psfphot`, which provided us with the residuals of the PSF fit. The aperture radius, used to estimate the initial flux of each source, was set to 3 pixels in `psfphot`, with `fit_shape` = (5, 5). We used the PSF-matched images homogenized to the $F444W$ resolution.

PSF photometry assumes that the sources are point-like in each of these bands, which is not the case here. This implies that our residual images may also include emission from the aforementioned objects. The latter could lead to an overestimation of the fuzzy emission. However, this is not concerning since the purpose of this Appendix is to provide some insights into the fuzz features, as well as a range within which the SED-inferred properties of the tLRD can vary.

We used the `voronoi_2d_binning` method from the `vorbin` `Python` package in the residual images. This package is an implementation of the two-dimensional adaptive spatial binning method of Cappellari & Copin (2003). It utilizes Voronoi tessellations to bin data to a given minimum S/N, allowing us to define the regions contributing to the fuzz. We computed pixel-by-pixel photometry of each of these regions and combined them to produce the SED of the total fuzz. The photo-z was estimated using `EAzY`, and the SED-derived properties were computed as in Sec. 4.2. We show the photometry, best-fitting models, and SFH of the fuzz in Fig. A.1. According to our analysis, this is a $z \sim 0.8$ projection of $10^8\,M_\odot$, with $A_V = 0.07$ mag, and log SFR $[M_\odot/\mathrm{yr}] = -1.45$. It could be dynamically coupled with C2 and/or C3, at the same z.

To compute the correction for the tLRD photometry, we drew three one-pixel-width annuli, separated by half a pixel, around the $0.3''$ aperture. Looking at Fig. 1, we see that the tLRD is off-center from the fuzz. Part of the tLRD is not exposed to this emission, so we divided the annuli in half, assuming the left side is free from contamination. This allows us to estimate the fuzz flux with respect to the sky in each annulus. We took the mean value considering the three annuli. This was done for every filter, resulting in a more significant correction for the rest-frame UV than for the optical. However, this correction is small enough that the tLRD retains its blue UV slope. We show the effects of this correction on the tLRD photometry in Fig. A.2. The SED-derived parameters from `Bagpipes` based on the corrected photometry are log $M_\star/M_\odot = 8.98^{9.09}_{8.85}$, $A_V = 0.86^{0.94}_{0.77}$ mag, and log SFR$[M_\odot/\mathrm{yr}] = 0.95^{1.06}_{0.86}$. These are compatible with the estimates reported in Table 3, and the SFHs also match. Therefore, the presence of this fuzzy emission does not alter our results.

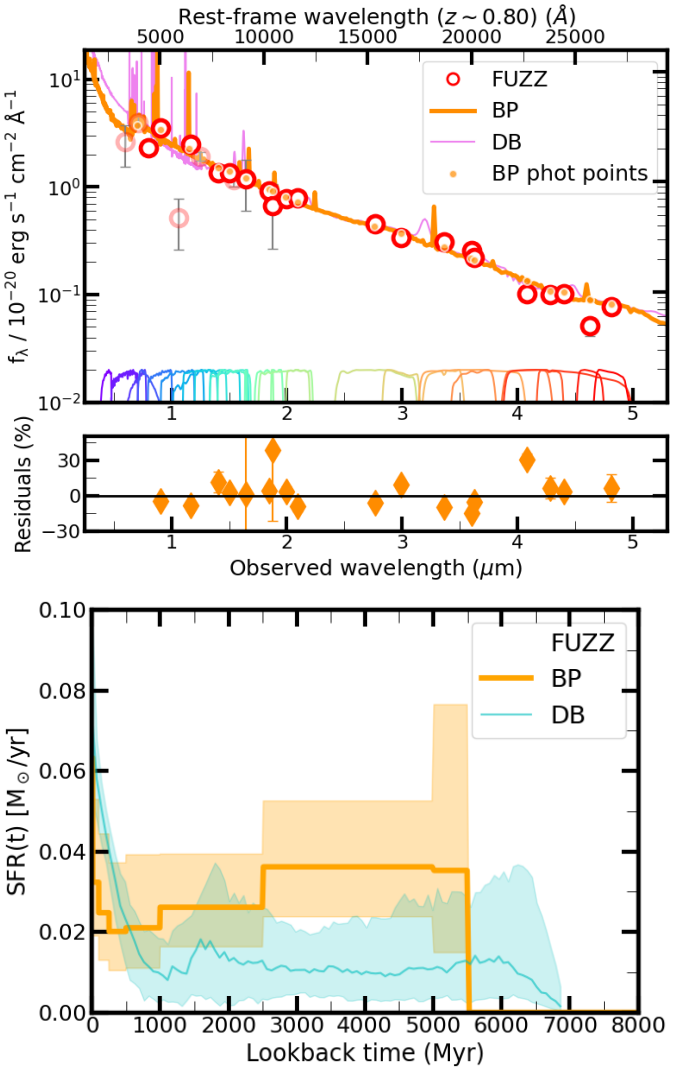

Fig. A.1: Top: photometry of the fuzzy emission (open red circles) and best-fitting models from `Bagpipes` and `Dense Basis` (in orange and violet). Check Fig. 2 for a complete description of the markers and color codes used in this plot. Bottom: SFHs derived with `Bagpipes` (orange) and `Dense Basis` (cyan). The shaded regions correspond to the area enclosed within the 16th and 84th percentiles.

Appendix B: The companions: C1, C2, and C3

We used `Bagpipes` and `Dense Basis` to fit the SEDs of C1, C2, and C3. Their photometry, best-fitting models, and SFHs are displayed in Fig. B.1. Table B.1 comprises their physical properties. C1 is the only source that could be at $z \sim 5$ according to these codes. We observe a dropout from $F090W$ to $F070W$, which is consistent with the Lyman break at $z \sim 5$. There is also a hint of [OIII] emission at $z \sim 5$ in the $F300M - F335M$ image (see Fig. 1). However, the contamination due to the tLRD makes its fitting and interpretation quite challenging.

Appendix C: `Bagpipes` and `Dense Basis` priors

In Table C.1 we show the values for the priors used in `Bagpipes` and `Dense Basis`.

Appendix D: Testing AGN priors

In order to test the consistency of our SED-derived properties in the case of tLRD, we forced different AGN solutions by changing the α_λ and β_λ priors. The original AGN solution, using broad priors for both parameters (see Table C.1), yielded

Table B.1: Best-fitting parameters of the companions derived using `Bagpipes` and `Dense Basis`.

ID	log $M_\star/M_\odot$	log SFR [$M_\odot$/yr]	A_v [mag]	log $M_\star/M_\odot$	log SFR [$M_\odot$/yr]	A_v [mag]
	`Bagpipes`			`Dense Basis`		
C1	$8.69^{8.75}_{8.65}$	$0.70^{0.74}_{0.67}$	$0.61^{0.65}_{0.57}$	$9.04^{9.24}_{9.04}$	$0.70^{0.98}_{0.70}$	$0.43^{0.49}_{0.43}$
C2	$8.00^{8.13}_{7.90}$	$-0.75^{-0.60}_{0.91}$	$0.14^{0.25}_{0.05}$	$8.10^{8.38}_{7.53}$	$-0.71^{-0.56}_{-0.97}$	$0.23^{0.46}_{0.07}$
C3	$8.45^{8.57}_{8.36}$	$-0.93^{-0.72}_{-1.19}$	$0.23^{0.42}_{0.08}$	$8.50^{8.61}_{8.32}$	$-1.13^{-0.74}_{-2.22}$	$0.22^{0.46}_{0.06}$

Notes. We include the 16th and 84th percentiles. The star formation rates correspond to SFR_{100}.

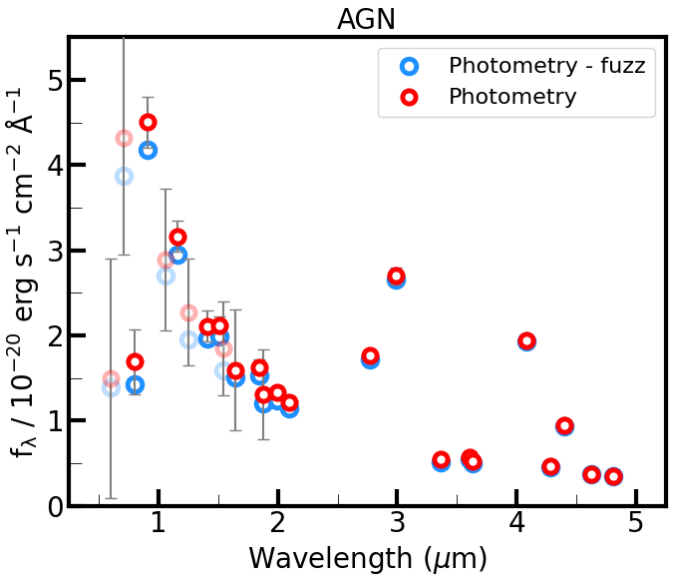

Fig. A.2: Effect of the fuzz correction on the tLRD photometry. The original photometry is shown as open red circles while the corrected values are displayed as open blue circles.

Table C.1: Priors used in this work.

`Bagpipes`	
SFR:	
log $Z/Z_\odot$	(0.001, 2.5)
log $M_{\star,\mathrm{formed}}/M_\odot$	(6,13)
Bin edges [Myr]	(0, 10, 100, 250 500, 800, 1100)*
A_V [mag]	(0, 2)
log U	(0, −4)
AGN:	
α_λ	(−2.5, 3)
β_λ	(−1.5, 2.3)
`Dense Basis`	
log $M_\star/M_\odot$	(6, 13)
Dust prior	Flat
sSFR prior	sSFRflat
log sSFR	(−12, −7.5)

Notes. *The bin edges shown in the table were used for the $z = 5$ sources, namely the tLRD, BBG, SAT1, and C1. For C2, C3, and the fuzz, we included bins at 2500, 5000, and 5500 Myr. We set a Calzetti et al. (2000) dust attenuation law in both codes. The redshifts were set to the z_{spec} (or photo-zs in the absence of spectra).

$\alpha_\lambda = -1.43, \beta_\lambda = 0.64$. The seed and final $M_\star$ are $10^{7.4}\,M_\odot$ and $10^{9.1}\,M_\odot$, respectively.

As a result of our tests we got four alternative fits, which we called Tests 1, 2, 3, and 4:

- Test 1: $\alpha_\lambda = -2.34, \beta_\lambda = -1.36, M_{\star,\mathrm{seed}} = 10^{7.7}\,M_\odot$, $M_{\star,\mathrm{final}} = 10^{9.1}\,M_\odot$
- Test 2: $\alpha_\lambda = 0.85, \beta_\lambda = -1.30, M_{\star,\mathrm{seed}} = 10^{7.9}\,M_\odot$, $M_{\star,\mathrm{final}} = 10^{9.1}\,M_\odot$
- Test 3: $\alpha_\lambda = 0.78, \beta_\lambda = 1.93, M_{\star,\mathrm{seed}} = 10^{7.3}\,M_\odot$, $M_{\star,\mathrm{final}} = 10^{9.1}\,M_\odot$
- Test 4: $\alpha_\lambda = -2.30, \beta_\lambda = 1.89, M_{\star,\mathrm{seed}} = 10^{7.2}\,M_\odot$, $M_{\star,\mathrm{final}} = 10^{8.9}\,M_\odot$

The final $M_\star$ estimates are all consistent with the resuls provided in Table 3. The seed masses are slightly less massive in Tests 3 and 4, and more massive in Tests 1 and 2. We show the corresponding SFHs in Fig. D.1.

All tests match the overall trend depicted by the tLRD's SFH, displayed in Fig. 8. They show larger uncertainties than the original fit for $t > 10$ Myr (especially Tests 3 and 4), but reflect upturns at 10 and 100 Myr which cannot be explained by secular evolution alone. Tests 3 and 4 place tLRD below the MS $\sim$ 500 Myr ago. The upturn taking place 100 Myr ago would have moved tLRD above the MS. It is important to remember that these are forced solutions in which we restricted the priors to explore different regimes of the AGN parameters.

These tests show that, depending on the priors, the relative intensities of the upturns seen in the SFH may vary, but the scenario depicted by the trends remains as described in Sect. 5.1. 100 and 10 Myr ago, tLRD experienced an increase in the star formation likely induced by the interaction and AGN triggering. The final mass of tLRD is $10^9\,M_\odot$. The seed mass is more uncertain, but it is $< 10^8\,M_\odot$.

The fact that the SFH and the $M_\star$ do not vary much when the AGN model assumptions are changed highlights the important role played by the stellar component in the fitting of this galaxy, as also reflected by the strong [OIII] + Hβ emission in this source (see Figs. 1 and 2).

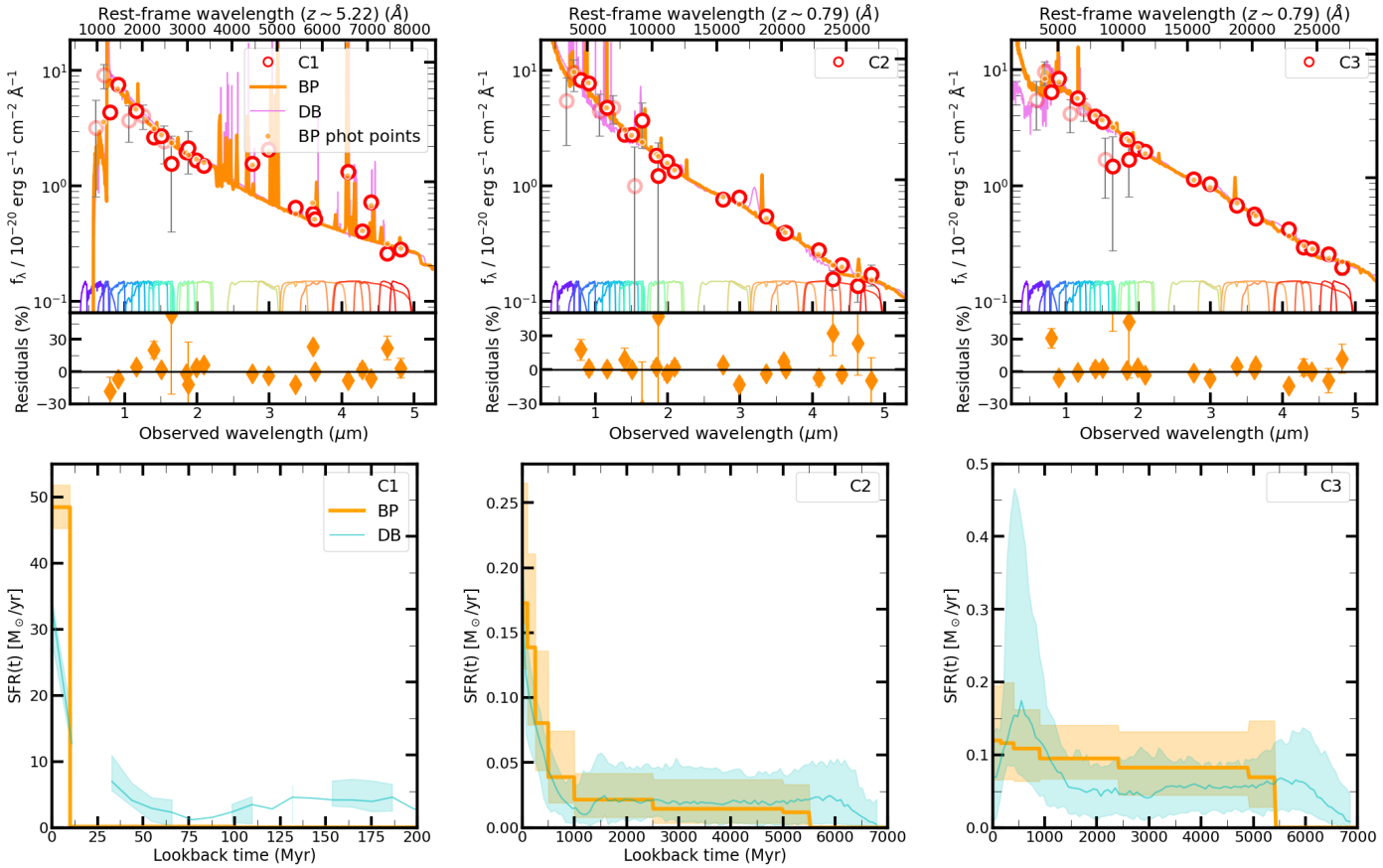

Fig. B.1: Top: photometry and SED fitting of C1 (left), C2 (middle), and C3 (right). See Fig. 2 for a complete description of the markers and color codes used in this plot. Bottom: SFHs of these objects, following the same order.

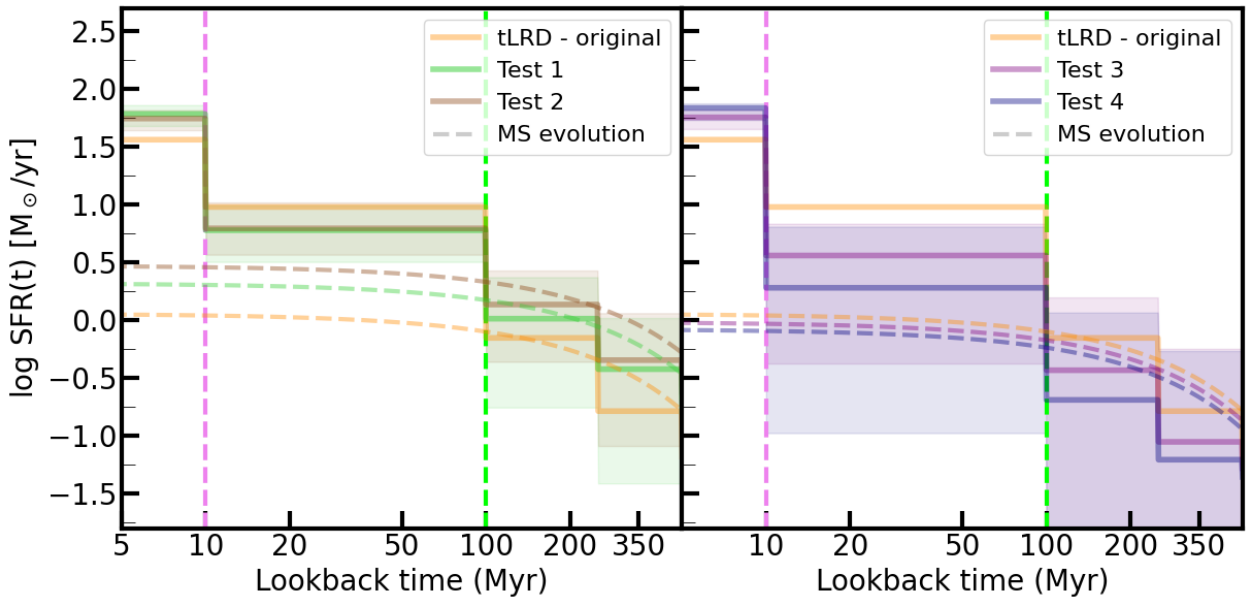

Fig. D.1: Original SFH of tLRD (solid orange), and SFHs obtained from our tests (green, brown, purple, and navy) on log scale. We divide the figure in two panels, each showing the results of two tests. SFHs of analogous galaxies evolving along the main sequence since $t = 500$ Myr ago are also depicted. The shaded region shows the SFH uncertainty. We do no include the uncertainty for the original SFH solution for the sake of clarity. Vertical lines highlight $t = 10$ Myr (violet) and $t = 100$ Myr (lime), respectively.